

Simulation of casting, homogenization, and hot rolling: consecutive process and microstructure modelling for aluminium sheet production

L Neumann^{1,4}, R Kopp¹, A Ludwig^{2,5}, M Wu^{2,5}, A Bührig-Polaczek²,
M Schneider³, M Crumbach³ and G Gottstein³

¹ Institut für Bildsame Formgebung, RWTH Aachen University, Aachen, Germany

² Gießerei-Institut, RWTH Aachen University, Aachen, Germany

³ Institut für Metallkunde und Metallphysik, RWTH Aachen University, Aachen, Germany

E-mail: neumann@ibf.rwth-aachen.de

Received 12 June 2003

Published 19 December 2003

Online at stacks.iop.org/MSMSE/12/S19 (DOI: 10.1088/0965-0393/12/1/S02)

Abstract

An overview of simulation of casting, homogenization, and hot rolling of an aluminium alloy is addressed in this paper. The microstructure models used to describe casting, solidification, precipitation (growth and coarsening) during homogenization, deformation texture evolution, and the work hardening behaviour are presented as well as their respective theoretical backgrounds. Emphasis is placed on interfacing the microstructure models with each other between the processing steps. This makes it possible to take into account microstructural changes that occur early during processing during later production steps. Along with this overview, reference will be made to previously presented simulation and experimental results—for validation—where appropriate.

1. Introduction

The process of production of aluminium sheets is divided into casting, solidification, heat treatment, and forming. All these stages of the production process were simulated with physically based models. The models have been validated by comparison with experimental processing.

In this paper, the authors' main emphasis lies in description of the models and the coupling strategy that has been developed so far (table 1). This strategy aims at describing each processing stage by its most important microstructural phenomena while taking the previous processing stage into account and thus creating a through process modelling approach. The associated results have been presented elsewhere as referred to in the text.

⁴ Author to whom any correspondence should be addressed.

⁵ Now with: Institut für Eisenhüttenkunde, Montanuniversität Leoben, Austria.

Table 1. Brief overview of the main (simulated and measured) results of each process step. These are handed to the next step, where they are input for the models.

Results of simulations	Necessary measurements
<i>Convection during solidification</i>	
<i>Microstructure evolution during solidification</i>	
Grain size	
Grain density	Grain size distribution and
Phase fraction	phase distribution
Microsegregation	
<i>Heat treatment of alloys</i>	
Phase fraction	
Mean radius	Texture
Solute element concentrations	
<i>Forming</i>	
Deformation texture	
Strain hardening	
Recrystallized volume fraction	Flow curves
Resulting forces and torques	

2. Solidification and casting structure formation

A two-phase globular equiaxed solidification model considering both grain movement and melt convection was developed [1–6]. The conservation equations, source terms, exchange terms, and some auxiliary terms are shown in table 2.

The liquid and solid phases are transported according to the mass conservation equation (1), taking solidification into account through a mass transfer term, M_{ls} ($=M_{sl}$), which is defined in equation (7). The volume fractions of both phases are subject to $f_l + f_s = 1$. Momentum exchange, \vec{U}_{ls} ($=-\vec{U}_{sl}$), in equation (2) consists of two parts: one due to mass transfer, \vec{U}_{ls}^p , and the other due to drag force, \vec{U}_{ls}^d . Details about the drag force model are given elsewhere [1, 3]. The solute concentration in the liquid and solid is calculated by solving equation (3). The solute partitioning at the liquid–solid interface due to phase change, C_{ls}^p , is taken into account, while the solute diffusional exchange at the liquid–solid interface C_{ls}^d is neglected. A mix concentration, c_{mix} , is defined in equation (11) to describe the macrosegregation. The enthalpy conservation equation (4) for both phases are also solved separately, and hence we get two different temperatures, T_l and T_s . With a relatively large diffusional heat exchange term, Q_{ls}^d , between the liquid and solid phases, the temperature difference can be levelled out, and a thermal equilibrium ($T_l \approx T_s$) is obtained. The enthalpy difference ($h_l - h_s = \Delta h_f$) defines the latent heat. Details of how the latent heat is handled in this model are also described previously [1, 3]. An additional conservation equation (5) is solved to obtain the grain density distribution, n . The grains are transported according to \vec{u}_s . An empirical three-parameter nucleation law (equation (6)) is used [7]. With the known n and f_s , the averaged grain size, d_s , is estimated by equation (12).

The conservation equations are solved with a control-volume based finite difference method. With this two-phase solidification model all the necessary volume-averaged variables describing the globular equiaxed solidification are obtained: temperature, T , and constitutional undercooling, ΔT , nucleation rate, N , grain density, n , and grain size, d , grain movement velocity, \vec{u}_s , and melt convection velocity, \vec{u}_l , concentrations in solid phase, c_s , and liquid phase, c_l . This model was applied to study the solidification and structure formation of the

Table 2. Conservation equations, source and exchange terms, and auxiliary equations for the numerical model of globular equiaxed solidification.

<i>Conservation equations</i>	
Mass:	$\frac{\partial}{\partial t}(f_l \rho_l) + \nabla \cdot (f_l \rho_l \vec{u}_l) = M_{sl} \quad (1)$
	$\frac{\partial}{\partial t}(f_s \rho_s) + \nabla \cdot (f_s \rho_s \vec{u}_s) = M_{ls}$
Momentum:	$\frac{\partial}{\partial t}(f_l \rho_l \vec{u}_l) + \nabla \cdot (f_l \rho_l \vec{u}_l \otimes \vec{u}_l) = -f_l \nabla p + \nabla \cdot \bar{\tau}_l + f_l \rho_l \vec{g} + \vec{U}_{sl} \quad (2)$
	$\frac{\partial}{\partial t}(f_s \rho_s \vec{u}_s) + \nabla \cdot (f_s \rho_s \vec{u}_s \otimes \vec{u}_s) = -f_s \nabla p + \nabla \cdot \bar{\tau}_s + f_s \rho_s \vec{g} + \vec{U}_{ls}$
	where $\bar{\tau}_l = \mu_l f_l (\nabla \otimes \vec{u}_l + (\nabla \otimes \vec{u}_l)^T)$ and $\bar{\tau}_s = \mu_s f_s (\nabla \otimes \vec{u}_s + (\nabla \otimes \vec{u}_s)^T)$
Species:	$\frac{\partial}{\partial t}(f_l \rho_l c_l) + \nabla \cdot (f_l \rho_l \vec{u}_l c_l) = \nabla \cdot (f_l \rho_l D_l \nabla c_l) + C_{sl} \quad (3)$
	$\frac{\partial}{\partial t}(f_s \rho_s c_s) + \nabla \cdot (f_s \rho_s \vec{u}_s c_s) = \nabla \cdot (f_s \rho_s D_s \nabla c_s) + C_{ls}$
Enthalpy:	$\frac{\partial}{\partial t}(f_l \rho_l h_l) + \nabla \cdot (f_l \rho_l \vec{u}_l h_l) = \nabla \cdot (f_l k_l \nabla \cdot T_l) + Q_{sl} \quad (4)$
	$\frac{\partial}{\partial t}(f_s \rho_s h_s) + \nabla \cdot (f_s \rho_s \vec{u}_s h_s) = \nabla \cdot (f_s k_s \nabla \cdot T_s) + Q_{ls},$
	where $h_l = \int_{T_{ref}}^{T_l} c_{p(l)} dT + h_l^{ref}$ and $h_s = \int_{T_{ref}}^{T_s} c_{p(s)} dT + h_s^{ref}$
Grain transport:	$\frac{\partial}{\partial t} n + \nabla \cdot (\vec{u}_s n) = N \quad (5)$
<i>Source terms</i>	
Nucleation:	$N = \frac{d\Delta T}{dt} \cdot \frac{n_{max}}{\sqrt{2\pi} \cdot \Delta T_\sigma} \cdot \exp\left(-\frac{1}{2} \cdot \left(\frac{\Delta T - \Delta T_N}{\Delta T_\sigma}\right)^2\right) \quad (6)$
<i>Exchange terms</i>	
Mass transfer:	$M_{ls} = g_\alpha \cdot \Delta c \cdot (n \cdot \pi d_s^2) \cdot \rho_s \cdot f_l \quad (7)$
Momentum:	$\vec{U}_{ls} = \vec{U}_{ls}^d + \vec{U}_{ls}^p \quad \vec{U}_{ls}^p = \vec{u}^* \cdot M_{ls} \quad \vec{U}_{ls}^d = K_{ls}(\vec{u}_l - \vec{u}_s) \quad (8)$
Species:	$C_{ls} = C_{ls}^d + C_{ls}^p \quad C_{ls}^p = c^* \cdot M_{ls} \quad C_{ls}^d \text{ neglected} \quad (9)$
Enthalpy:	$Q_{ls} = Q_{ls}^d + Q_{ls}^p \quad Q_{ls}^p = h^* \cdot M_{ls} \quad Q_{ls}^d = H^* \cdot (T_l - T_s) \quad (10)$
<i>Auxiliary terms</i>	
Mix concentration:	$c_{mix} = \frac{c_l \cdot \rho_l \cdot f_l + c_s \cdot \rho_s \cdot f_s}{\rho_l \cdot f_l + \rho_s \cdot f_s} \quad (11)$
Grain diameter:	$d_s = \left(\frac{6 \cdot f_s}{\pi \cdot n}\right)^{1/3} \quad (12)$
Solid viscosity:	$\mu_s = \begin{cases} \frac{\mu_l}{f_s} \cdot \left(\left(1 - \frac{f_s}{f_s^c}\right)^{-2.5 \cdot f_s^c} - (1 - f_s)\right) & \text{when } f_s < f_s^c \\ \infty & \text{else} \end{cases} \quad (13)$

industrial alloy AlCu₄Mg. With Ti as grain refiner, the morphology of the solidified primary phase was handled as a sphere.

The simulation and experimental evaluation procedures of the ingot (plate) casting are shown in figure 1. The melt, with pouring temperature 700°C, is poured into a metal (steel) die with mould preheating of 300°C. The temperature distribution after mould filling is then transferred to the two-phase globular equiaxed solidification model. The heat exchange coefficient at the casting die interface is 800 W m⁻² K⁻¹. A convection heat exchange boundary condition on the top surface of the casting was applied; the convection heat transfer coefficient is taken as 50 W m⁻² K⁻¹ and the environmental temperature as 10°C.

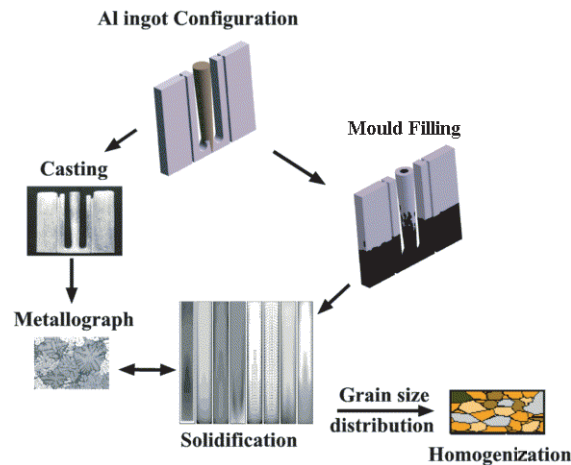


Figure 1. Mould filling and solidification simulations. Casting trials are made to evaluate the simulation results. The predicted grain size distribution is further transferred to the subsequent homogenization model.

The solidification shrinkage and the thermal-solutal convection are ignored for this case, but the grain sedimentation and the sedimentation-induced convection are considered with the Boussinesq approach. Both grain sedimentation and the sedimentation-induced melt convection are found to have a strong influence on the final grain size distribution. Details of the solidification and structure evolution processes were previously analysed in [2, 6]. The fine grain size ($\sim 262 \mu\text{m}$) at the bottom region is mainly due to the high nucleation rate in the initial stage and partially due to the sedimentation. The largest grains ($\sim 390 \mu\text{m}$) are predicted near the surface regions, about 30–40 mm above the bottom. Those large grains are actually transported from the upper regions. After nucleation in the upper regions, they sink downwards. They grow while sinking and finally reach a large grain size during their relatively long travel. The relatively small grains predicted in the central region are due to the melt currents, which transport the fine grains from the bottom regions upwards to the centre.

For validation, experimental castings were performed. The castings were sectioned, and specimens were taken at different positions. The microscopic metallographic examinations were made with Barker etching, and the grain size was measured manually at equal intervals (2 mm) across the casting sections. Around each measuring point, ten random grains were selected and the grain size was averaged. The grain size distribution in the real casting agrees reasonably well with the numerical prediction [2]. The casting section was also energy dispersive x-ray (EDX) analysed for macrosegregation. The experimentally measured data are relatively scattered. It is difficult to compare the experimental data with the numerical results quantitatively. However, the measured result shows the same tendency as the simulation: there is a lower concentration in the casting bottom region and a higher concentration in the top region. Considering the complexity of the equiaxed solidification process, the above agreement is found to be encouraging.

In addition to the above macrostructure simulation, the micro-macro coupling is made to calculate the microstructure parameters such as the phase fraction, dendrite arm spacing, and microsegregation [8]. The temperature field in the casting can be obtained by solving the enthalpy conservation equation under a system scale. A one-dimensional FDM microsimulation module is implemented in the main solver to calculate the microstructure parameters locally. The macrotemperature distribution and the local cooling rate serve as

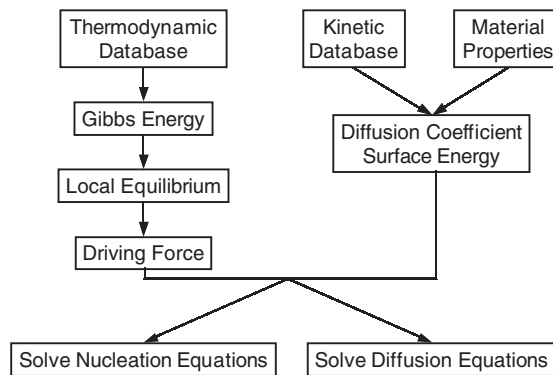


Figure 2. General overview of the model. The combination of thermodynamic and kinetic data has enabled the user to address the time dependent evolution of the precipitation process.

inputs for the micromodule. As feedback, the release of latent heat and the change in the heat capacity, which are determined by the change of phase fraction and phase concentration in the microsimulation module, will be passed to the macrotemperature simulation. In order to determine the local liquid–solid interface equilibrium information, a thermodynamic software (Thermo-Calc) is used. Simulations on the same plate casting as shown in figure 1 were made. It was found that the numerical predictions correspond to the experimentally observed phase fractions and dendritic arm spacing.

3. Homogenization

The homogenization process was modelled within the framework of classical nucleation theory and deterministic rules for the growth and coarsening of precipitates, as originally proposed by Zener [9]. Therefore, a statistical model for precipitation processes has been developed by Schneider *et al* [10]. The growth law for a single precipitate includes growth from the supersaturated matrix as well as coarsening due to the Gibbs–Thomson effect. Combining the nucleation rate and the growth law in the continuity equation makes it possible to describe the evolution of the whole precipitate size distribution. Since an analytical solution of this partial non-linear inhomogeneous differential equation cannot be obtained, it was solved numerically in a manner similar to that postulated by Kampmann and Wagner [11]. This approach makes sure that the information of the whole size distribution is considered. The model is capable of describing the simultaneous nucleation, growth, and coarsening of several types of spherical precipitates. In contrast to simulations taking into account local diffusion fluxes on a spatial grid (e.g. Cahn–Hilliard simulations), the present algorithm is fast and therefore of particular interest for industrial applications.

The input parameters for the model can be subdivided into two groups. On the left-hand side of figure 2, we start with the thermodynamic database. In the regular case, these databases contain parameters to describe the Gibbs energy functions for all phases of the alloy system. To obtain the values of the equilibrium state, the elements must be spread to all phases in order to minimize the Gibbs energy of the whole system.

To calculate the equilibrium phases, the chemical driving forces, and the equilibrium concentrations, the commercial Gibbs energy minimizer ChemApp [12] and a thermodynamic database (COST 507 [13]) were embedded. The main advantage of this strategy is that there is nearly no restriction to a special alloy system. Further on, the model is capable of describing

the mentioned alloy system with respect to the phase diagram and the latent heats over the whole range of temperature and concentrations. We just have to assume that the system has been investigated and that the thermodynamic database is available.

As the equilibrium state describes the behaviour of the alloy system only after an infinite amount of time, kinetic data and material properties must also be considered to obtain the time dependence of the precipitation process. Only physically based parameters have been used to describe the precipitation kinetics. These parameters, such as diffusion data and interface energies, have to be taken from the literature [14, 15].

3.1. Homogenization model description

The activation energy for nucleation consists of three parts, namely the chemical free energy, $\Delta G(c)$, arising from the chemical supersaturation of the solutes, the interfacial energy, ΔG_I , spent for creating the precipitation/matrix interface, and the strain energy, ΔG_S , used to accommodate the strain mismatch. As the thermodynamic data are measured in terms of heat capacities, the sum of $\Delta G(c)$ and ΔG_S is given as the transformation energy, ΔG_T , represented as the latent heat, Δg_T , per unit volume. Therefore, the Gibbs energy for each precipitate reads as

$$\Delta G = -\Delta G_T + \Delta G_I \quad \text{or} \quad \Delta G = -V \cdot \Delta g_T + S \cdot \sigma \quad (14)$$

V is the volume and S the surface of the precipitate. Assuming spherical nuclei, we obtain the critical radius, r_c , from the first derivative of the Gibbs energy function. Now, the nucleation rate per second can be calculated according to Becker and Döring [16]:

$$\dot{N} = N_0 \cdot Z \cdot \beta \cdot \exp\left(-\frac{\Delta G(r_c)}{k_B \cdot T}\right) \quad (15)$$

N_0 represents the maximum possible number of nuclei. T is the temperature, $n^2(r_c)$ the number of atoms per nucleus, and k_B the Boltzmann constant. The Zeldovich factor, Z , is a normalization variable that can be expressed according to Kampmann and Wagner [11]. The rate, β , at which solute atoms join the critical radius may be calculated according to [17, 18]. For this calculation the following values are necessary: D , the diffusion coefficient of the slowest diffusing element, $c(t)$, its current matrix concentration, and λ , the lattice parameter.

To set off nucleation, we added a Gaussian distribution to the existing size distribution. The growth and coarsening of the precipitates can be calculated according to Zener [19]:

$$\frac{dr}{dt} = \frac{c(t) - c^\alpha(r)}{c^\beta - c^\alpha(r)} \cdot \frac{D}{r} \quad (16)$$

The growth law for a single precipitate includes its growth from the supersaturated matrix, $c(t)$, as well as coarsening due to the Gibbs–Thomson effect. From the equilibrium concentration of the precipitates, c^β , and the Gibbs–Thomson concentration, $c^\alpha(r)$ [20],

$$c^\alpha(r) = c^\alpha \exp\left(\frac{1 - c^\alpha}{c^\beta - c^\alpha} \cdot \frac{2 \cdot \Delta\sigma \cdot V_M^\beta}{R_G \cdot T} \cdot \frac{1}{r}\right) \quad (17)$$

where c^α and c^β are the equilibrium concentrations of the matrix and the precipitate, V_M^β is the molar volume of the precipitating phase, and R_G is the gas constant. Combining the nucleation rate and the growth law in the continuity equation, it is possible to describe the evolution of the whole precipitate number and size distribution, $f(r, t)$.

$$\frac{\partial f(r, t)}{\partial t} + \frac{\partial}{\partial r} \left(\frac{dr}{dt} \cdot f(r, t) \right) = \dot{N} \quad (18)$$

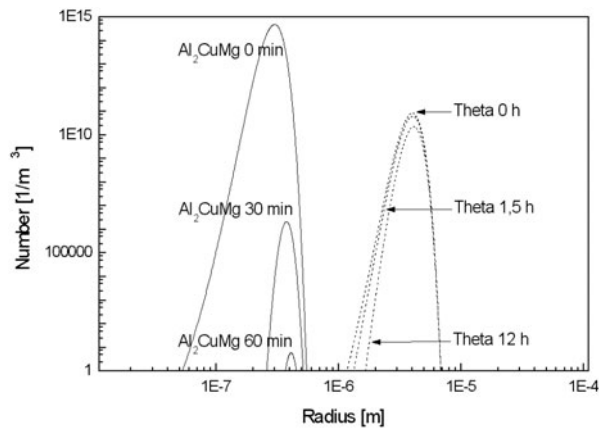


Figure 3. Simulated evolution of number and size distributions of second-phase particles during homogenization (alloy: lab-cast AA2024).

Since an analytical solution of this partial non-linear inhomogeneous differential equation cannot be obtained, it was solved numerically in a manner similar to that postulated by Kampmann and Wagner [11]. This approach makes sure that the information on the whole number and size distribution is considered. Since all equations are given in a differential way with respect to time, non-isothermal conditions can be treated as small steps of isothermal conditions.

The results of this type of simulation are the number and size distributions of second-phase particles and the chemical composition of the matrix phase (figure 3). These results are used as input (see also table 1) for the three-internal-variable model (3IVM), which calculates the flow stress in subsequent forming steps (e.g. rolling). As described in the following section, these data are used mainly to quantify statistically the obstacles' distance for dislocation movement.

4. Forming

After homogenization of aluminium alloys, the next step in industrial production of sheet metal is hot rolling. The key to accurate, predictive modelling of forming processes is correct calculation of the flow stress, k_f . The flow stress is stress determined by uniaxial compression tests (with minimized friction). Its evolution is governed by a multitude of physical hardening and softening mechanisms, of which the most important (by influence on k_f) are taken into consideration by the 3IVM [22]. Crystallographic texture also influences the flow stress evolution, and its description during forming is currently a subject of greater interest as it affects the forming behaviour of sheets by causing plastic anisotropy. The models applied and the linking strategy between them are described in the following.

Recent results of simulations that were carried out with the modelling scheme described in this section are presented by Neumann *et al* [21].

4.1. Three-internal-variable model

Metals with high stacking fault energies such as Al and its alloys tend to build cellular dislocation substructures. In contrast to cold forming, such a structure is observed after hot deformation in the case of Mg alloyed aluminium also. A model capable of representing such a

structure was developed by Roters *et al* [22]. This model is referred to as the 3IVM. Like other previously published statistical one- [23, 24] and two-parameter [25, 26] models, the 3IVM consists of a kinetic equation of state and a set of equations that account for the description of the microstructural evolution.

The 3IVM describes the dislocation substructure by considering three populations of dislocation densities: the immobile dislocations in the interior of the cells (ρ_i), the immobile dislocations in the cell walls (ρ_w), and the mobile dislocations (ρ_m). Because of their motion, the mobile dislocations are considered to be the carriers of plastic strain in the crystal. The evolution of each of these dislocation densities is described by an equation of the following form:

$$\dot{\rho}_x = \rho_x^+ - \rho_x^- \quad (19)$$

where x is m, i, or w, depending on which population of dislocation densities is considered. The Orowan equation is used as the kinetic equation of state for calculating the external stress:

$$\dot{\gamma} = \dot{\epsilon} \cdot \bar{M} = \rho_m \cdot b \cdot v_{\text{glide}} \quad (20)$$

where $\dot{\gamma}$ is the shear rate, $\dot{\epsilon}$ the imposed strain rate, \bar{M} the average polycrystal Taylor factor, b the magnitude of the Burgers vector, and v_{glide} the average velocity of dislocation movement by glide. The dislocation velocity is calculated assuming stress-assisted and thermally activated overcoming of short-range obstacles:

$$v_{\text{glide}} = \lambda \cdot \nu_0 \cdot \exp\left(-\frac{Q}{k_B \cdot T}\right) \cdot \sinh\left(\frac{\tau_{\text{eff}} \cdot V}{k_B \cdot T}\right) \quad (21)$$

where λ is the jump width, ν_0 the attack frequency, Q the effective activation energy for overcoming obstacles, and V the activation volume. Furthermore, k_B is the Boltzmann constant and τ_{eff} is the effective stress. The activation energy used is an effective value. It includes the different effects of passing short-range obstacles: cutting of forest dislocations and dragging of jogs and solute atoms. The jump width corresponds to the mean obstacle distance. Since recently, the spacing of solute atoms is also taken into account by the 3IVM next to the spacing of forest dislocations in cell walls and interiors for calculation of λ . For this, Goerdeler and Gottstein [27] proposed a linear reciprocal superposition of the different obstacle spacings:

$$\frac{1}{\lambda_x} = \sqrt{\rho_x} + \frac{1}{l_F} \quad (22)$$

The subscript x is either i or w, denoting the values obtained for the cell interiors and walls, respectively. l_F represents the Friedel length, which is used to quantify the effective spacing of solute atoms. Though this is a very basic approach to solute hardening, it has proven to be extremely useful for predicting the influence of solute contents on flow stress [27].

Accordingly, the effective stresses, τ_{eff} , in cell walls and interiors can be calculated for a set of given strain rate, temperature, and dislocation densities. The athermal stress contribution caused by long-range dislocation interaction is added, resulting in the total shear stresses, $\tau_{i,w}$, that are calculated as

$$\tau_{i,w} = \tau_{\text{eff},i,w} + \alpha \cdot G \cdot b \cdot \sqrt{\rho_{i,w}} \quad (23)$$

Then, the flow stress, k_f , is calculated as the weighted sum of the total shear stresses of both volume fractions:

$$k_f = \bar{M} \cdot (f_i \cdot \tau_i + f_w \cdot \tau_w) \quad (24)$$

where f_i and f_w are the volume fractions of the cell interiors and walls, respectively.

The 3IVM is implemented into an implicit FE software. The FE code calls up the 3IVM for each finite element of the workpiece at each Gauss point in each iteration. The local values

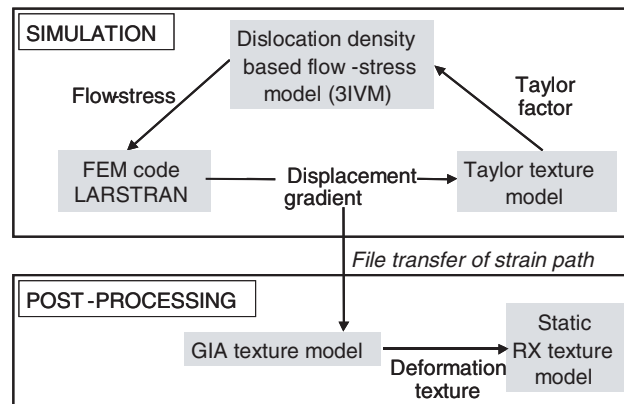


Figure 4. Micro–macro coupling strategy for hot and cold forming simulations of aluminium alloys.

for alloy composition, Taylor factor, temperature, strain, and strain rate are transferred to the 3IVM by the FE code, which in turn calculates the dislocation density evolution, starting from the values calculated in the previous increment. Then, the flow stress is returned to the FE code by the 3IVM, allowing feedback of the dislocation density evolution on the material stiffness in the FE model. Furthermore, a texture model (briefly described below) is used to calculate the average Taylor factor in each element incrementally. The value of the Taylor factor is used by the 3IVM in the flow stress calculation and implicitly in the calculation of k_f (see also figure 4).

4.2. Deformation texture

The plastic flow of a metal does not depend solely on dislocation interaction but also on the crystallographic orientation of the grains in the workpiece. The distribution of the grain orientations weighted by their volume fractions is referred to as the texture of the material. In metal forming processes, the grain orientations change, and it can be observed that grains rotate into certain preferred orientations for an imposed strain path (e.g. rolling). This causes a deformation texture, which in turn causes anisotropic flow behaviour of the material in subsequent forming operations, especially in deep drawing [28]. The knowledge and understanding of material flow is important for avoiding defective products and reducing prototyping time in die design.

The grain orientation in reference to the macroscopic coordinate system (e.g. sheet) is defined by the three Euler angles. The change in grain orientation is caused by lattice rotation during forming [29]. A material's texture changes throughout the forming process, starting from the initially measured texture, which must be taken into account for prediction of texture evolution (see table 1).

4.3. Simulation with full constraints Taylor model

A number of models capable of describing the evolution of deformation texture have been developed in the past [30]. A model very frequently referred to was developed by Taylor [31]. The most important restriction of the Taylor model is the compatibility of distortion, meaning that a single grain has to undergo the same distortion as a macroscopic sample. This is why

the classical Taylor model is also referred to as a full constraints model (FC model). In the present simulations, it was used solely for interactive calculation of the Taylor factor, which represents the influence of texture on flow stress evolution in the 3IVM. The Taylor factor of a single grain amounts to

$$M = \frac{\sum_{i=1}^s |d\gamma_i|}{d\varepsilon_V} \quad (25)$$

with incremental equivalent macroscopic strain $d\varepsilon_V$, $d\gamma_i$ the incremental amount of slip on a slip system i , and s the number of slip systems. \bar{M} can then be calculated as the volume-weighted average of all orientations in the polycrystal. The value of \bar{M} is passed on to the 3IVM (figure 4). Implementation of the Taylor model into the FE code has been presented by Aretz *et al* [32, 33].

Comparisons of different deformation texture models have shown that for face-centred cubic metals the FC Taylor model shows only rough qualitative agreement with measured rolling textures [34]. However, the evolution of \bar{M} , which is on its own a rather rough statistical description of the texture, is only slightly influenced by this deviation, so that in the described interactive framework of FEM, 3IVM, and FC Taylor, the simple FC Taylor model does perform well and operates time-efficiently for capturing the effect of texture evolution on strain hardening (figure 4).

For a detailed description of the texture evolution, more sophisticated models are used. Due to the high computational demands of such models, they are run in postprocessing and only for certain areas that are of special interest in a workpiece (e.g. centre and surface of slab/sheet during rolling). Therefore, the strain path of the respective elements of the FE mesh, which describes their deformation history, is transferred to the deformation texture model.

4.4. Simulation with grain interaction model in postprocessing

In order to achieve the above-mentioned more precise prediction of deformation textures, models have been developed allowing for locally heterogeneous deformations of the material, in contrast to the FC Taylor model. One such model is the so-called GIA model [35]. The GIA model considers intergranular interactions by describing an eight-grain aggregate embedded in a homogeneous medium. The deformation of the complete aggregate is fully prescribed, as for single grains in the classical FC Taylor model. For each grain of the GIA model, all shear and strain components in the strain rate tensor, $\dot{\varepsilon}_{ij}$, are relaxed, and so each grain can deform differently according to its kinematic hardness (Taylor factor). This causes strain incompatibilities among the grains, which are removed by the introduction of geometrically necessary dislocations (GNDs), causing additional deformation energy. By adding the GND energies and the Taylor energies for slip on the active slip systems in all eight grains, the total energy for the deformation of the aggregate is described. Minimizing this total energy delivers the amount of relaxation, the active slip systems, and the amount of slip on them—thus the orientation change in each grain.

The input texture for the model has to be discretized into a number, N_0 , of single orientations. These orientations are assumed to be randomly distributed among $N_0/8$ aggregates of eight grains. Each cluster is then treated separately. It is important to mention that the model is strongly material dependent. The elastic constants, grain size, and shape as well as crystal structure are accounted for by the model. Measured or modelled work hardening curves serve as inputs to the model and indirectly reflect different deformation conditions with respect to temperature, strain rate, and chemical composition, which strongly influence the texture predictions [36, 37].

Recent comparisons have demonstrated the outstanding performance of the GIA model [34, 38]. Considering the much higher computational demands of similarly performing crystal plasticity FE models makes GIA a most powerful tool for complicated texture simulations throughout a process with various deformation steps, as e.g. described in [39, 40]. Besides, a system is under development to determine nuclei spectra for recrystallization with the GIA model, which establishes a close link to recrystallization modelling [41].

5. Conclusions and outlook

5.1. Solidification and casting structure formation

A two-phase volume averaging model is successfully used to simulate the solidification in an aluminium ingot casting including nucleation, grain evolution, grain movement, sedimentation, melt convection, solute transport, and macrosegregation. Through micro–macro coupling, it is able to calculate the other microstructure parameters, such as the phase fraction, dendrite arm spacing, and microsegregation. Satisfactory agreement between the simulations and the experiments is found. This indicates that the experimentally observed microstructure and its formation mechanisms can be well explained with numerical simulations; the numerical model can be further developed as a tool to predict and control microstructure.

5.2. Homogenization

This processing stage is modelled taking simultaneous nucleation, growth, and coarsening of several types of spherical precipitates into account. The grain size, grain density, phase fraction, and microsegregation calculated by the model for casting and solidification are input parameters for this model.

5.3. Forming

The strain hardening (via dislocation density modelling) and deformation texture models utilized as well as the coupling strategies applied were presented. The input parameters from the homogenization model to the forming models are the phase fraction, the mean radius of precipitates, and the solute element concentrations. Furthermore, the model coupling techniques applied were presented.

5.4. Outlook

In the future, cold forming will become the last step of production in the process chain presented. Cold rolling and deep drawing of a cup will be the last stages described. The texture calculated during hot rolling will be an input of importance for this step as a texture-based yield locus is to be used in order to predict the plastic anisotropy during sheet metal forming (the earing profile in this case).

Acknowledgments

The authors gratefully acknowledge the financial support of the Deutsche Forschungsgemeinschaft (DFG) within the Collaborative Research Centre (SFB) 370 ‘Integral Materials Modelling’. Furthermore, the support of the colleagues active within SFB 370, especially B Pustal (Gießerei-Institut), H Aretz (Institut für Bildsamer Formgebung), and M Goerdeler

(Institut für Metallkunde und Metallphysik) was essential for the achievements presented in this paper.

References

- [1] Ludwig A and Wu M 2002 Modeling of globular equiaxed solidification with a two phase approach *Metall. Mater. Trans. A* **33** 3673–83
- [2] Wu M and Ludwig A 2003 Influence of phase transport phenomena on macrosegregation and structure formation during solidification *Adv. Eng. Mater.* **5** 62–6
- [3] Wu M, Ludwig A, Bührig-Polaczek A, Fehlbier M and Sahn P R 2003 Influence of convection and grain movement on globular equiaxed solidification *Int. J. Heat Mass Transfer* **46** 2819–32
- [4] Ludwig A, Wu M, Ehlen G and Sahn P R 2000 Numerical description of solid movement during equiaxed solidification using a two-phase modeling approach *Oral Presentation and Proc. in Materials Week 2000 (Munich, Germany, 25–28 September 2000)* www.materialsweek.org
- [5] Wu M, Ludwig A, Sahn P R and Bührig-Polaczek A 2002 Prediction of grain distribution and macrosegregation: an example of Al-4.0% Cu plate casting *Oral Presentation and Proc. in Materials Week 2002 (Munich, Germany, 30 September–2 October 2002)* www.materialsweek.org
- [6] Wu M, Ludwig A, Sahn P R and Bührig-Polaczek A 2003 Grain evolution and macrosegregation in Al-4.0%Cu casting—simulation and experimental evaluation *Accepted for Oral Presentation (Proceedings in press) in McWASP-X (Modeling of Casting, Welding and Advanced Solidification Processes) (Florida, 25–30 May 2003)*
- [7] Rappaz M 1989 Modelling of microstructure formation in solidification processes *Int. Mater. Rev.* **34** 93–123
- [8] Pustal B, Böttger B, Ludwig A, Sahn P R and Bührig-Polaczek A 2003 Simulation of macroscopic solidification with an incorporated one-dimensional microsegregation model coupled to thermodynamic software *Met. Mater. Trans. B* **34** 411
- [9] Zener C 1949 *J. Appl. Phys.* **20** 950–3
- [10] Schneider M, Gottstein G, Löchte L and Hirsch J 2002 A statistical model for precipitation—applications to commercial Al–Mn–Mg–Fe–Si alloys *Proc. ICAA8 2002* vol II, ed P J Gregson and S J Harris (Hrsg.) (Trans Tech Publications) pp 637–42 *8th International Conf. on Aluminum Alloys (Cambridge, UK)* pp 02.-5.07
- [11] Kampmann R and Wagner R 1983 *Decomposition of Alloys: the Early Stages* (Oxford: Pergamon) pp 91–103
- [12] For more information and publications see <http://gttserv.lth.rwth-aachen.de/gtt>
- [13] European Commission COST 507 Thermochemical database for light metal alloys, V1-3, ISBN 92-828-3901-X, 92-828-3902-8, 92-828-3903-6
- [14] Landolt-Börnstein, New Series III/26, p 151
- [15] Howe J M 1997 *Interfaces in Materials* 1997, ISBN 0-471-13830-4
- [16] Becker R and Döring W 1938 *Ann. Phys.* **32** 128
- [17] Wagner R and Kampmann R 1991 Phase transformation in materials *Materials Science and Technology* vol 5 (New York: VCH) pp 213–303
- [18] Aaronson H I and Lee K J 1975 *Lecture on the Theory of Phase Transformations* (The Metallurgical Society) pp 83–115
- [19] Zener C 1949 *J. Appl. Phys.* **20** 950–3
- [20] Gibbs J W 1948 *Collected Works* (New Haven, CT: Yale University Press)
- [21] Neumann L, Aretz H, Kopp R, Goerdeler M, Crumbach M and Gottstein G 2003 *Z. Metallkd.* **94** 593
- [22] Roters F, Raabe D and Gottstein G 2000 *Acta Mater.* **48** 4181
- [23] Kocks U F 1976 *J. Eng. Mater. Technol.* **98** 76
- [24] Mecking H and Kocks U F 1981 *Acta Metall.* **29** 1865
- [25] Estrin Y and Mecking H 1984 *Acta Metall.* **32** 57
- [26] Zehetbauer M 1993 *Acta Metall.* **41** 589
- [27] Goerdeler M and Gottstein G 2001 *Proc. Recrystallization and Grain Growth (Aachen, Germany)* vol II, ed G Gottstein and D A Molodov, (Berlin: Springer) p 987
- [28] Banabic D, Bunge H-J, Pöhlandt K and Tekkaya A E 2000 *Formability of Metallic Materials* (Berlin: Springer)
- [29] Fischer-Bühner J 1998 *PhD Thesis* RWTH Aachen University (Aachen: Shaker-Verlag)
- [30] Van Houtte P 1996 *Proc. ICOTOM 11 (Xian, China)* ed Z Liang *et al* (Beijing: International Academic Publishers) p 236
- [31] Taylor G I 1938 *J. Inst. Met.* **62** 307
- [32] Aretz H, Luce R, Wolske M, Kopp R, Goerdeler M, Marx V, Pomana G and Gottstein G 2000 *Modelling Simul. Mater. Sci. Eng.* **8** 881

- [33] Aretz H, Luce R, Wolske M, Kopp R, Goerdeler M, Pomana G and Gottstein G 2001 *J. Phys. IV (France)* **11** 115
- [34] Van Houtte P, Delannay L, Bate P and Engler O 2002 *Proc. PLASTICITY '02—Plasticity, Damage and Fracture at Macro, Micro and Nano Scales (Palm Beach, Aruba)* ed A S Kahn and O Lopez-Pamies (Fulton, Maryland: Neat Press) p 278
- [35] Crumbach M, Pomana G, Wagner P and Gottstein G 2001 *Proc. Recrystallization and Grain Growth (Aachen, Germany)* vol II, ed G Gottstein and D A Molodov (Berlin: Springer) p 1053
- [36] Crumbach M, Mukhopadhyay P, Aretz H, Pomana G, Wagner P and Gottstein G 2001 *Proc. Recrystallization and Grain Growth (Aachen, Germany)* vol II, ed G Gottstein and D A Molodov (Berlin: Springer) p 1061
- [37] Engler O 2000 *Acta Mater.* **48** 4827
- [38] Crumbach M, Gottstein G, Löchte L, Piot D, Driver J, Allen C M and Savoie J F 2002 *Mater. Sci. Forum* 396–402 357
- [39] Goerdeler M, Crumbach M, Gottstein G, Neumann L, Luce R, Kopp R, Allen C M, v d Winden M and Karhausen K F 2002 *Mater. Sci. Forum* **396–402** 379
- [40] Goerdeler M, Crumbach M and Gottstein G 2002 *Proc. ICOTOM (Seoul)* vol 13
- [41] Crumbach M, Goerdeler M and Gottstein G 2002 *Proc. ICOTOM (Seoul)* vol 13